Available online at www.sciencedirect.com

ScienceDirect

Proceedings of the Combustion Institute 39 (2023) 1647–1656

Proceedings of the Combustion Institute

www.elsevier.com/locate/proci

Spherical gas-fueled cool diffusion flames

Minhyeng Kim [a], Kendyl A. Waddell [a], Peter B. Sunderland [a,*], Vedha Nayagam [b], Dennis P. Stocker [c], Daniel L. Dietrich [c], Yiguang Ju [d], Forman A. Williams [e], Phillip Irace [f], Richard L. Axelbaum [f]

[a] *Department of Fire Protection Engineering, University of Maryland, College Park, MD 20742, United States of America*
[b] *Department of Mechanical and Aerospace Engineering, Case Western Reserve University, Cleveland, OH 44106, United States of America*
[c] *NASA Glenn Research Center, Cleveland, OH 44135, United States of America*
[d] *Department of Mechanical and Aerospace Engineering, Princeton University, Princeton, NJ 08544, United States of America*
[e] *Department of Mechanical and Aerospace Engineering, University of California at San Diego, La Jolla, CA 92093, United States of America*
[f] *Department of Energy, Environmental and Chemical Engineering, Washington Univ. in St. Louis, St. Louis, MO 63130, United States of America*

Received 5 January 2022; accepted 2 July 2022
Available online 1 August 2022

Abstract

An improved understanding of cool diffusion flames could lead to improved engines. These flames are investigated here using a spherical porous burner with gaseous fuels in the microgravity environment of the International Space Station. Normal and inverse flames burning ethane, propane, and *n*-butane were explored with various fuel and oxygen concentrations, pressures, and flow rates. The diagnostics included an intensified video camera, radiometers, and thermocouples. Spherical cool diffusion flames burning gases were observed for the first time. However, these cool flames were not readily produced and were only obtained for normal *n*-butane flames at 2 bar with an ambient oxygen mole fraction of 0.39. The hot flames that spawned the cool flames were 2.6 times as large. An analytical model is presented that combines previous models for steady droplet burning and the partial-burning regime for cool diffusion flames. The results identify the importance of burner temperature on the behavior of these cool flames. They also indicate that the observed cool flames reside in rich regions near a mixture fraction of 0.53.
© 2022 The Combustion Institute. Published by Elsevier Inc. All rights reserved.

Keywords: Formaldehyde; Intensified video camera; Microgravity combustion; Porous burner

1. Introduction

Cool premixed flames were discovered in the 1800s. Initially thought to be only a novelty, their

* Corresponding author.
E-mail address: pbs@umd.edu (P.B. Sunderland).

https://doi.org/10.1016/j.proci.2022.07.015
1540-7489 © 2022 The Combustion Institute. Published by Elsevier Inc. All rights reserved.

study increased dramatically when they were found to be responsible for knock in internal combustion engines [1,2].

Cool diffusion flames were first observed only in the last decade. In these flames the fuel and oxidizer are supplied from opposite sides and arrive at the flame via diffusion, whereas in cool premixed flames the flames propagate into a premixture. The equivalence ratios and temperature distributions of the two flame types are so different that a full understanding of cool flame chemistry will require studies in both premixed and diffusion flames.

Cool flames are different from their hot flame counterparts in that: their peak temperatures are only 500 – 1000 K [3]; they increase the gas temperature by only 2 – 200 K [4]; they only consume a small fraction of the reactants; and they produce primarily H_2O, CO, H_2O_2, CH_2O, and C_2H_4 [5], see also [1,6,7]. Cool flames are possible only under conditions with negative-temperature coefficients (NTCs) in the overall reaction rate. Such NTCs are near the crossover temperature, for which alkyl radicals are consumed at equal rates by cool and hot flame chemistry.

Cool flames are of practical interest because their low-temperature combustion (LTC) chemistry may contribute to the improvement of advanced high-efficiency engine technologies, such as homogeneous charge compression ignition (HCCI), premixed charge compression ignition (PCCI), and reactivity controlled compression ignition (RCCI) [2,8–11].

Cool diffusion flames were discovered in *n*-heptane droplet combustion experiments aboard the International Space Station (ISS) [6]. Additional cool diffusion flames burning droplets in microgravity were observed for *n*-heptane, *n*-octane, *n*-decane, *n*-dodecane, and decane/hexanol mixtures [12–15]. In most cases the cool diffusion flames appeared soon after the radiative extinction of a hot flame, but they were sometimes ignited directly by a resistively heated wire [2,11]. Some of the cool diffusion flames led to hot flame ignitions. The cool diffusion flames burned for up to 35 s before extinguishing [2,6,11]. Extensive modeling of these flames has been performed [7,11,14].

The existence of counterflow cool diffusion flames was predicted by Law and co-workers [8,16]. These flames were subsequently observed in normal gravity for *n*-butane, isobutane, *n*-heptane, *n*-octane, *n*-decane, *n*-dodecane, *n*-tetradecane, dimethyl ether, and diethyl ether at various pressures [3,10,17–20]. Owing to the short residence times available in counterflow flames, they required LTC enhancements such as heated reactants, pulsed plasmas, and ozone addition [3,17].

Counterflow multistage warm diffusion flames, with peak temperatures around 1000 K, were discovered soon after [11,14,21,22]. These have been observed for *n*-heptane, *n*-decane, *n*-dodecane, and dibutyl ether.

Burner-supported quasi-spherical cool diffusion flames in normal gravity were observed and modeled by [23,24]. These involved dimethyl ether with diluents and pressures chosen to minimize gravitational interference. Turbulent jet cool diffusion flames were investigated experimentally and numerically for dimethyl ether and diethyl ether [20,25].

Despite extensive past work, gaps remain in the understanding of cool diffusion flames. Droplet studies cannot control or precisely measure the fuel supply rate or become fully steady. They also do not allow for fuel dilution, inverse flames, or gaseous fuels. Furthermore, their detailed models are complicated by the liquid phase. Counterflow flames cannot obtain the low strain rates and long residence times of spherical diffusion flames, have small length scales that complicate measurements, and require heated reactants, plasma, and/or ozone assistance. Normal gravity spherical diffusion flames are affected by buoyant entrainment, especially outside the flame. The spherical cool diffusion flames studied here avoid these shortcomings. They are not perfect, however; for example, the support tube is a thermal mass that quenches the system, and the burner temperature is not easily controlled.

Thus motivated, the objectives of this study are to use a spherical porous burner with gaseous fuels to observe spherical hot and cool diffusion flames in microgravity and to develop a simple model of these flames. Three alkane fuels are considered – ethane, propane, and *n*-butane – as are normal and inverse flames. A wide range of flow rates and nitrogen dilution of the fuel and oxidizer are studied at various pressures. The flame size measurements are compared with model predictions.

2. Experimental

These experiments are part of the Cool Flames Investigation with Gases (CFI-G) project. The tests were performed aboard the ISS inside the Combustion Integrated Rack (CIR) using the Advanced Combustion via Microgravity Experiments (ACME) insert. A windowed pressure vessel with a free volume of 83 L provided quiescent ambient conditions. This facility is described in more detail in [26].

A 6.4 mm diameter spherical porous burner, shown in Fig. 1, was located near the center of the pressure vessel. The burner was fabricated from sintered 316 stainless steel with 10 μm media, and has an estimated porosity of 40%. Several effects of the burner and its support tube on similar flames are discussed in [26]. The burner temperature was measured using an embedded type K (nickel/chromium/alumel) thermocouple. Tests

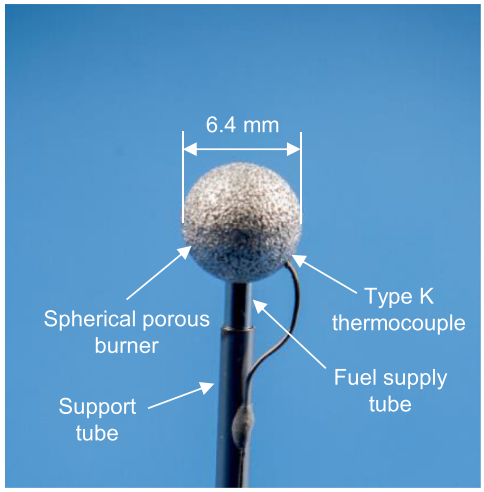

Fig. 1. The spherical porous burner prior to testing.

were terminated if the burner reached 723 K to prevent overheating. A retractable hot wire ignited the flames.

Two types of diffusion flames were observed: normal flames, with the fuel flowing from the burner toward the oxidizer, and inverse flames, with the oxidizer flowing toward the fuel.

The fuels were ethane, propane, and *n*-butane, and they were generally diluted with N_2. For propane and *n*-butane inverse flames the fuel supply was two-phase. The oxidizer was O_2, which was diluted with N_2. The burner gas flow rates were controlled with mass flow controllers with an estimated uncertainty of ± 5%.

A summary of the test conditions is provided in Table 1, where $\dot{m}_{HC}$ and $\dot{m}_{O2}$ are the mass flow rates of hydrocarbon and O_2, p is ambient pressure, and X is mole fraction. The uncertainty of the burner and ambient gas mole fractions is estimated at ± 0.02 and ± 0.01, respectively. The ambient temperature was 298 K. The test conditions were generally varied as widely as permitted by safety requirements and the hardware. The variations in ambient pressure, temperature, and concentrations during these tests were negligible.

The tests were recorded and monitored in real time using an analog color camera at 30 frames/s (fps). This was not sensitive enough to image the cool flames, so a digital monochrome intensified camera was also used, at 23 fps. It had a bandpass filter of 390 – 490 nm to admit light from excited formaldehyde (CH_2O^*), which dominates the visible emissions from cool flames.

For some flames a type B (platinum/rhodium) thermocouple measured gas temperatures. This had a wire diameter of 0.2 mm and was at a radius of 13 mm. Grayscale thin filament pyrometry (TFP) was attempted with 14 μm diameter SiC fibers using the method of Irace et al. [26].

A Schmidt-Boelter wide-angle thermopile radiometer measured radiative emissions. This was at a radius of 154 mm and was sensitive to wavelengths of 0.6 – 50 μm. Two other radiometers, at 0.2 – 17.5 μm, confirmed these measurements. Three wide-angle photomultiplier tubes (PMTs) measured optical emissions with bandpass filters of 230 – 700, 310, and 430 nm, but these were only marginally able to detect the cool flames. A transducer measured chamber pressure. Additional details of the hardware and diagnostics are in [26,27].

3. Analytical

Analytical models are derived here that relate the flame radii of burner-supported hot and cool diffusion flames to global parameters such as boundary temperatures, flow rates, and gas compositions.

The Spalding model of droplet burning [28] assumes: a quasi-steady fuel flow rate; unity Lewis number; constant product of density, ρ, and mass diffusivity, D; uniform and constant pressure; and negligible radiation heat transfer. Note that radiation and unsteadiness can be reasonably accounted for with an appropriate choice of transport rates. This has been demonstrated for studies of spheri-

Table 1
Summary of the hot and cool flames observed.

Fuel	Flame type	X_{O2}	X_{HC}	p (bar)	$\dot{m}_{HC}$ or $\dot{m}_{O2}$[a] (mg/s)	# of RE[b]	# of FT[c]	# of cool flames
ethane	normal	0.18 - 0.4	0.25 – 1	0.51 - 2.03	0.50 - 2.36	30	10	0
propane[d]	normal	0.21 - 0.4	0.05 – 1	0.94 - 3.04	0.13 - 2.89	34	6	0
n-butane	normal	0.21 - 0.4	0.02 - 0.5	0.51 - 2.03	0.10 - 3.22	46	17	15
ethane	inverse	0.12 - 0.85	0.06 - 0.3	0.46 - 3.04	0.93 - 9.08	25	22	0
propane	inverse	0.18 - 0.85	0.08 - 0.43	0.51 - 3.04	1.36 - 9.07	24	13	0
n-butane	inverse	0.21 - 0.85	0.06 - 0.36	0.51 - 3.04	1.34 - 8.95	30	23	0

[a] $\dot{m}_{HC}$ for normal flames and $\dot{m}_{O2}$ for inverse flames.
[b] RE indicates radiatively extinguished.
[c] FT indicates flow terminated.
[d] For propane normal flames at pressures above 1 bar, X_{O2} was limited to 0.21.

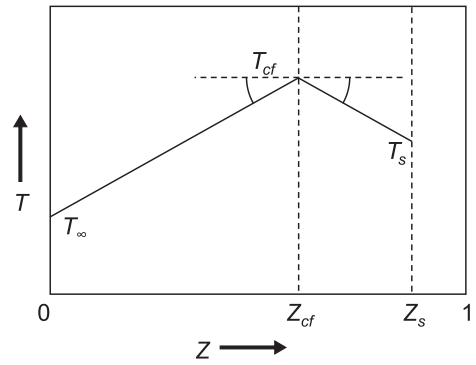

Fig. 2. Temperature T versus mixture fraction in the partial-burning regime for a normal cool diffusion flame, reproduced from Nayagam et al. [28].

cal burner-supported flames [26] and droplet flames [5–7,11–15,28–31].

This model is extended here to burner-supported hot diffusion flames and cool diffusion flames. Conservation of mass and mixture fraction become

$$\rho\, v\, r^2 \;=\; \rho_s\, v_s\, r_s^2, \tag{1}$$

and

$$\rho\, v\, r^2\, \frac{dZ}{dr} \;=\; \frac{d}{dr}\left(r^2\, \rho\, D\, \frac{dZ}{dr} \right), \tag{2}$$

where r is radius, s is the burner surface, v is velocity, and Z is mixture fraction.

An infinitely thin control volume at the burner surface, with inflow, outflow, and outward diffusion of Z, yields the burner boundary condition:

$$\rho_s\, v_s = \; \rho_s\, v_s\, Z_s - \rho_s\, D_s\, \frac{dZ}{dr}\,|_s \tag{3}$$

The first integration of Eq. (2) is facilitated with conservation of mass. Including the burner boundary condition then yields

$$\frac{dZ}{dr} = \frac{-\,v}{D}\,(\,1\,-\,Z\,) \tag{4}$$

Assuming constant ρD and using Eqs. (1), (4) is readily integrated. The boundary condition at infinity for normal flames ($Z \to 0$ as $r \to \infty$) is then applied, yielding

$$\frac{v_s\, r_s^2}{D_s\, r} \;=\; ln\left(\frac{1}{1\,-\,Z} \right), \tag{5}$$

and

$$\frac{\dot{m}}{4\,\pi\,\rho\,D\,r} \;=\; ln\left(\frac{1}{1\,-\,Z} \right), \tag{6}$$

where $\dot{m}$ is the total mass flow rate from the burner.

Evaluating Eq. (6) at the porous burner surface yields the burner surface mixture fraction,

$$Z_s = \;1\;-\;exp\!\left(\frac{-\,\dot{m}}{4\,\pi\,r_s\,\rho\,D} \right). \tag{7}$$

The hot flame stabilizes at the stoichiometric mixture fraction, Z_{st}. Solving Eq. (6) at this location yields the hot flame radius for normal flames,

$$r_{hf} = \frac{\dot{m}}{4\,\pi\rho\,D\,ln\left(\frac{1}{1\,-\,Z_{st}} \right)}. \tag{8}$$

Most cool diffusion flames do not reside at the stoichiometric location. Instead, their locations can be determined using temperature profiles in mixture fraction space as illustrated in Fig. 2. As discussed in [28], cool diffusion flames are in the partial-burning regime, which requires dT / dZ to

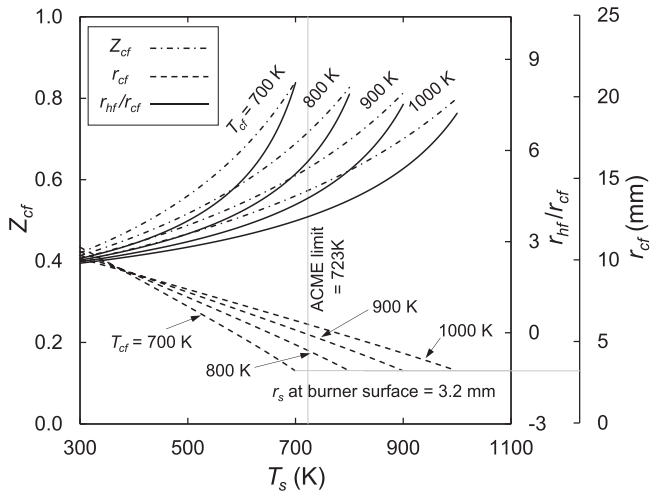

Fig. 3. Model predictions of normal cool diffusion flames for the conditions of $\dot{m}_{HC}$ = 1.5 mg/s, r_s = 3.2 mm, T_∞ = 300 K, Z_{st} = 0.20, and ρD = 0.0334 g/m-s at 300 K.

be opposite on the two sides of the flame. For normal cool diffusion flames this can be expressed as

$$\frac{Z_{cf}}{Z_s - Z_{cf}} = \frac{T_{cf} - T_\infty}{T_{cf} - T_s}, \tag{9}$$

where subscripts cf and ∞ denote the cool flame and the outer boundary. Rearranging yields

$$Z_{cf} = \frac{\left(T_{cf} - T_\infty\right) Z_s}{2\,T_{cf} - T_s - T_\infty}. \tag{10}$$

This relationship, along with its analog for inverse flames, shows that for both flame types the burner surface and the ambient must be cooler than the cool flame.

Equations (1)–(7) are valid for both hot and cool flames, and it is shown below that a single ρD at room temperature can be used for both flames by evaluating the value at their respective flame temperatures. Therefore, Eq. (6) can be evaluated for normal cool diffusion flames at $Z = Z_{cf}$ and $r = r_{cf}$ to obtain

$$r_{cf} = \frac{\dot{m}}{4\,\pi\,\rho\,D\,ln\left(\frac{1}{1 - Z_{cf}}\right)}, \tag{11}$$

with Z_{cf} given in Eq. (10). Finally, the ratio $r_{hf}\,/\,r_{cf}$ is found from Eqs. (8), (10), and (11) to be

$$\frac{r_{hf}}{r_{cf}} = \frac{ln\left(1 - Z_{cf}\right)}{ln\left(1 - Z_{st}\right)}$$

$$= ln\left[1 - \frac{\left(T_{cf} - T_\infty\right) Z_s}{2\,T_{cf} - T_s - T_\infty}\right] / ln\left(1 - Z_{st}\right) \tag{12}$$

Equations (1)–(12) apply not only to burner-supported flames, but also to quasi-steady droplet flames.

For inverse flames, the flame radii are found to be

$$r_{hf} = \frac{\dot{m}}{4\,\pi\,\rho\,D\,ln\left(\frac{1}{Z_{st}}\right)} \tag{13}$$

and

$$r_{cf} = \frac{\dot{m}}{4\,\pi\,\rho\,D\,ln\left(\frac{1}{Z_{cf}}\right)}. \tag{14}$$

Eqs. (12)–(14) show that, depending on the conditions, a normal or inverse cool flame can reside in rich or lean regions. When X_{O2} is large, any cool flame generally resides between the burner and the stoichiometric location.

Fig. 3 plots the predictions of Eqs. (10)–(12) for Z_{cf}, r_{cf}, and $r_{hf}\,/\,r_{cf}$ at conditions selected using experiments presented below. When $T_s = T_\infty$ (here 300 K), these quantities are nearly independent of T_{cf}. For other burner temperatures the cool flame size increases with T_{cf}. For increasing T_s, the cool flame shrinks monotonically until it collapses onto the burner when T_s reaches T_{cf}. The ACME burner temperature limit is indicated with a vertical line. A version of Fig. 3 for inverse diffusion flames is provided in [32].

4. Results

As summarized in Table 1, 280 hot diffusion flames were ignited. Following the ignition transient, these flames generally grew with time, with many reaching quasi-steady radii, as reported for similar flames by [26]. There were 189 flames that extinguished radiatively and the others extinguished when the flow was terminated, in some cases because the burner reached its temperature limit of 723 K.

Table 2
Summary of the cool flames observed[a].

Test[a, b]	$\dot{m}_{HC}$(mg/s)	cool flame duration(s)	r_{cf}(mm)	$r_{hf}\,/\,r_{cf}$
A	0.75	14.3	5.1	2.4
B	1.0	13.8	5.3	2.8
C[c]	1.0	13.6	–	–
D	1.5	13.9	7.6	2.3
E	1.5	13.8	7.5	2.3
F1	1.0	6.2	5.1	2.8
F2	1.0	5.8	5.5	2.7
F3	1.0	5.5	5.7	2.6
F4	1.0	5.4	5.7	2.6
F5	1.0	5.3	5.5	2.6
G1	1.5	10.9	7.1	2.4
G2	1.5	3.4	6.5	2.7
G3	1.5	3.8	6.3	2.8
G4	1.5	4	6.2	2.8
G5	1.5	3.7	6.2	2.9

[a] $X_{O2} = 0.39$, $X_{HC} = 0.3$, $p = 2$ bar, and $Z_{st} = 0.20$ for all tests. The adiabatic flame temperature was 2650 K.
[b] Numbered tests involved hot-cool-hot flame transitions.
[c] The cool flame radius for Test C could not be measured due to low camera gain.

When a flame extinguished radiatively, the flow was continued for at least 10 s to allow a possible transition to a cool diffusion flame. Despite the broad range of conditions, only 15 such cool flames ignited, as summarized in Table 2. The cool flames were imaged by the intensified camera except during Test C.

Fig. 4 shows a hot flame 10 s before its radiative extinction and the subsequent cool flame. Compared to the cool flame, the hot flame was larger, brighter, and more spherical and it had a thinner reaction zone. The hot flame also had a larger quenched region near the cold burner support tube.

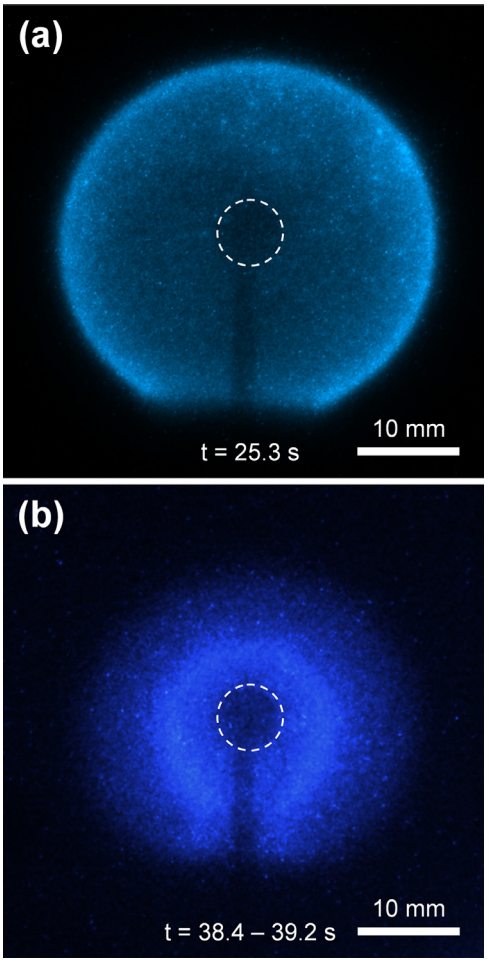

Fig. 4. Intensified camera images from Test D of (a) the hot flame and (b) the cool flame. The false colors here were obtained by matching the colors of microgravity hot flames and normal gravity cool flames. The times after ignition, t, are shown. The dashed circles indicate the burner location. Image (b) is an average of images from the times shown and has an exposure 50 times as bright as that of (a).

TFP was attempted only for Test C. (This precluded using the high gain in the intensified camera for this test.) No glow was detected in the filament, indicating the peak temperature was below the TFP detection limit of 950 K, which is consistent with a cool diffusion flame, but not with a hot flame.

Fig. 5a shows the radiometer signal, burner temperature, and burner flow rate for a representative normal flame undergoing radiative extinction without a cool flame. Flame oscillations began at 18 s and increased in strength until flame extinction at 30 s. The flow continued for an additional 14 s but no cool flame appeared in the intensified camera and the radiometer output followed an asymptote toward zero as the gas and burner cooled.

Fig. 5b plots the same quantities for Test D. The conditions were the same as in Fig. 5a except for the decreased flow rate. The smaller flame and the longer hot-flame burn time increased the burner temperature at the time of radiative extinction. This occurred at 36 s and a cool diffusion flame appeared at 37 s. (A similar delay, 0.7 – 1.1 s, occurred for all 15 cool flames.) The fuel flow was terminated at 50 s, whereby the cool flame extinguished. During the cool flame, the radiometer output and burner temperature were steady enough to suggest this flame would have lasted indefinitely with continued flow and an infinite domain.

The cool flames in Tests A – E were not detected in real time because the intensified camera images and the radiometer output were not available until later. Therefore, their flows were terminated prematurely. This was remedied prior to Tests F and G. At the same time the type B thermocouple was added, as required for a different ACME project.

Fig. 5c plots the same measurements for Tests G1 – G5. (These conditions are the same as those of Test D except for the addition of the type B thermocouple.) Here the hot flame radiatively extinguished at 40 s and a cool flame appeared at 42 s. However, the cool flame transitioned to a hot flame at 54 s due to the presence of the type B thermocouple. Five such cool flames, preceded and followed by hot flames, were observed until the flow was terminated at 165 s. The first hot and cool flames lasted longer than the others.

When each hot flame extinguished, the type B thermocouple was in a rich premixture and catalyzed exothermic reactions [33] that reignited the hot flame. These reignitions occurred for Tests F and G when the thermocouple reached 720 – 820 K and were confirmed by the intensified camera and the radiometer and burner temperatures. As shown in Fig. 5c, during each cool flame the type B thermocouple warmed and began to glow. These temperatures have not been corrected for radiative loss or catalysis because the radiation corrections are small at these temperatures, catalytic corrections are highly uncertain, and these measurements are used here primarily to show temperature trends.

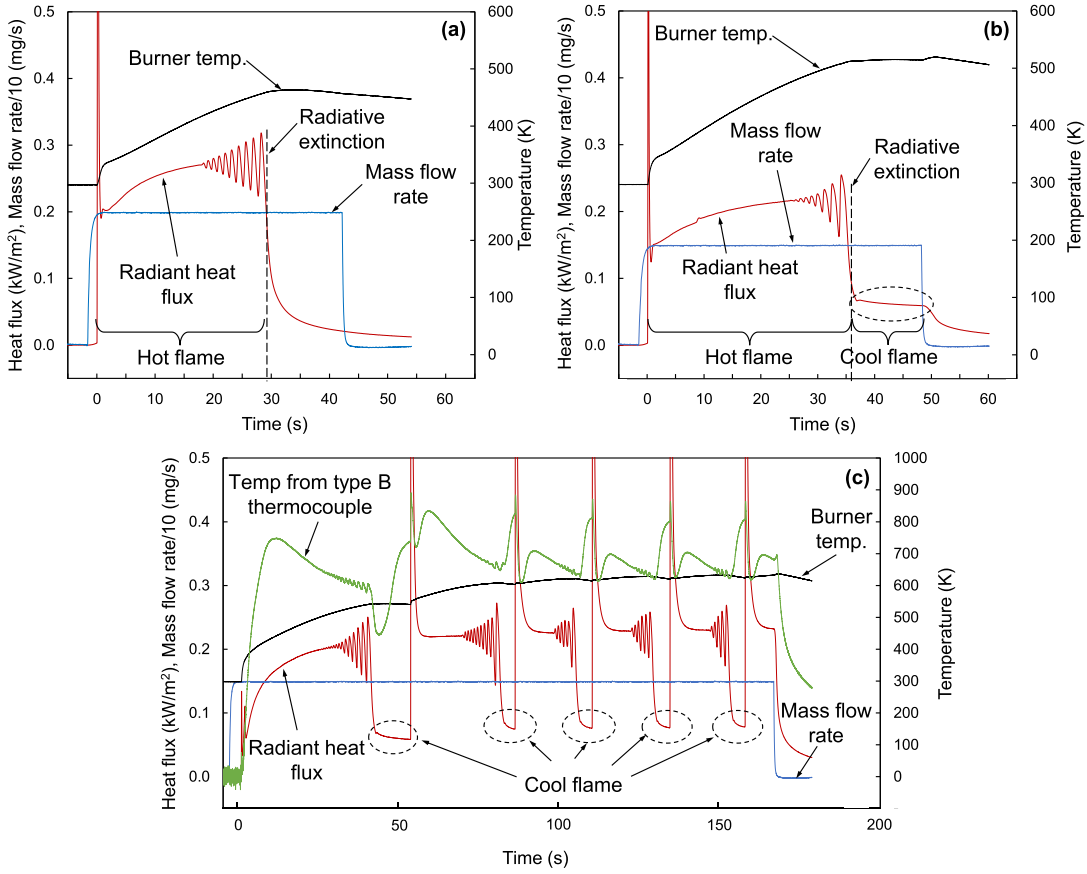

Fig. 5. Temporal plots of measurements for (a) a hot flame at $\dot{m}_{HC} = 2$ mg/s that extinguishes, (b) a hot flame at $\dot{m}_{HC} = 1.5$ mg/s that transitions to a cool diffusion flame (Test D), and (c) multiple hot-cool flame transitions at $\dot{m}_{HC} = 1.5$ mg/s (Tests G1-G5).

As indicated by Tables 1 and 2, these cool diffusion flames are only possible for very limited conditions. For example, cool diffusion flames were not observed for ethane or propane, nor at pressures below 2 bar. This is consistent with the understanding that higher alkanes [34] and higher pressures [2,10] favor cool flames.

Cool flames were not observed for inverse burning, primarily because of short residence times. The inverse flames also had low burner temperatures (below 500 K), but droplet cool diffusion flames are observed with surface temperatures near 400 K.

Cool flames were not observed for oxygen mole fractions below about 0.4, which is consistent with a limiting oxygen index for cool flames [35]. Cool flames were not seen for fuel mole fractions other than 0.3, $\dot{m}_{HC}$ outside the range of 0.75 – 1.5 mg/s, or when the burner was cooler than 515 K.

The intensified camera images were used to find flame radii for the tests of Table 2. These radii were invariant with time and their uncertainty is estimated at ± 2%. Hot flame images just prior to oscillations were analyzed by fitting the contour of peak blue intensity with a circle. Cool flame images were filtered to reduce noise and then averaged over 20 frames. Fig. 6 shows the resulting image for Test G1. Pixel values along a line through the burner center and perpendicular to the support tube identified two peaks, as plotted in Fig. 6. The cool flame radius was found as half their separation distance, as was done by [28] for droplet flames.

The measured flame radii are shown in Table 2. The mean measured r_{hf} / r_{cf} is 2.6 and the mean predicted by Eq. (12) is 3.2. Measurements from [13,28] for *n*-decane droplets indicate hot and cool flame standoff ratios of 8 and 3.2, i.e., $r_{hf} / r_{cf} = 2.5$. The model of [29] predicts this ratio to be 3 for an *n*-heptane droplet.

Fig. 7 plots the measured versus modeled hot and cool flame radii. This includes the cool flames of Table 2 and quasi-steady normal *n*-butane hot flames for various conditions of X_{O2} (0.37 – 0.40), X_{HC} (0.15 and 0.3), $\dot{m}_{HC}$ (0.75 – 2.0 mg/s), and pressure (0.5, 1, and 2 bar). The modeled radii are from

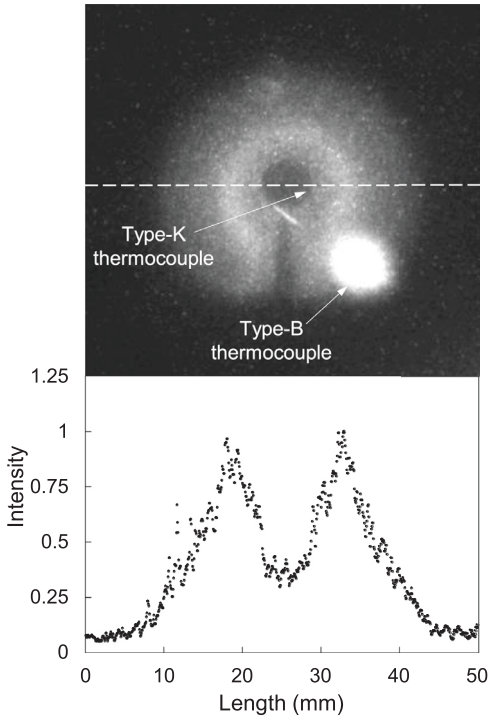

Fig. 6. Averaged image of the cool flame of Test G1 and a plot of the pixel values along the dashed line. The white streak in front of the burner tube is the type B thermocouple's double reflection off the camera lens and the window.

Eqs. (8) and (11). A peak cool flame temperature of 750 K is assumed, which is reasonable for alkanes [2,6,7,11,14,30,31].

Assuming peak temperatures of 1400 K for hot flames [26] and 750 K for cool flames, and using the data of Fig. 7, ρD was optimized to a value of 0.0334 g/m-s at 300 K. This value is assumed here to be constant for all hot and cool flames regardless of species. Wang et al. [36] found $\rho D = 0.0248$ g/m-s for an equimolar mixture of O_2 and N_2 at 1.01 bar and 298 K. Changing from the peak temperature to the mean would increase this value of 0.0334 g/m-s, whereas estimating and plotting the steady flame sizes in Fig. 7 would decrease it.

Fig. 7 indicates this model with $\rho D = 0.0334$ g/m-s is reasonably successful in predicting hot and cool diffusion flame radii for these conditions. Eq. (7) from the model indicates the mean Z_s for the cool flames of Table 2 is 0.75. The mean Z_{cf} is then found to be 0.53 from Eq. (11) and the measured radii. Finally, the mean T_{cf} is found from Eq. (10) to be 869 K. This temperature is higher than expected but is reasonable given the assumptions in the model.

5. Conclusions

Spherical diffusion flames burning gases were investigated aboard the ISS, emphasizing conditions suitable for cool diffusion flames. An analytical model to obtain flame radii was formulated for

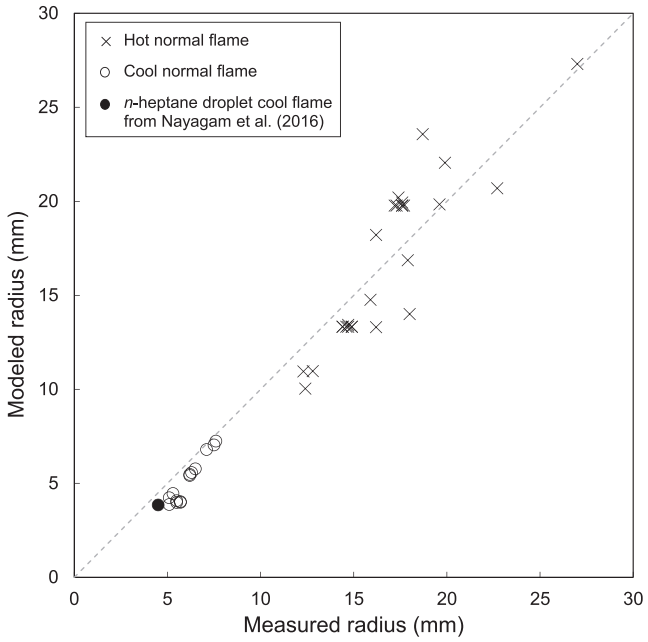

Fig. 7. Measured versus modeled flame radii for hot and cool flames. The droplet cool flame is from [28]. The data has a coefficient of determination of $R^2 = 0.92$ with respect to the line shown with unity slope.

hot and cool flames. The main conclusions are as follows.

1. Spherical cool diffusion flames burning gases were observed for the first time. Fifteen such flames were observed. They formed after the hot flame radiatively extinguished and were quasi-steady until the flow was terminated. When a type B thermocouple was present, the cool flames transitioned to hot flames, leading to cyclical hot and cool flames.
2. Cool diffusion flames for these fuels are not easily obtained. They were only observed for normal *n*-butane flames at 2 bar, and only for butane flow rates of 0.75 – 1.5 mg/s. In addition, these cool flames were only observed for burner temperatures above 515 K.
3. The cool diffusion flames are smaller than their hot flame counterparts, with a mean ratio of hot/cool flame radii of 2.6.
4. The cool flame peak temperatures were below the TFP detection limit of 950 K.
5. The analytical model, based on the Spalding model of droplet combustion and the partial-burning regime, reveals quantitatively the importance of burner temperature on the size and peak temperatures of cool diffusion flames.
6. The model indicates that a reasonable approximation for ρD for these hot and cool flames is $\rho D = 0.0334$ g/m-s at 300 K. The model also indicates that these cool flames reside in rich regions with a mixture fraction of 0.53, and that their surface mixture fraction is 0.75.

Declaration of Competing Interest

The authors declare that they have no known competing financial interests or personal relationships that could have appeared to influence the work reported in this paper.

Acknowledgments

This work was supported by NSF grant CBET-1740490 and the in-kind assistance of NASA and CASIS. The authors are grateful to the ISS crew members and the ISS operations team, particularly A. Adams and M. Smajdek, for their assistance. Helpful discussions with C.K. Law are appreciated.

References

[1] P.G. Lignola, E. Reverchon, Cool flames, Prog. Energy Combust. Sci. 13 (1987) 75–96.
[2] Y. Ju, C.B. Reuter, O.R. Yehia, T.I. Farouk, S.H. Won, Dynamics of cool flames, Prog. Energy Combust. Sci. 75 (2019) 100787.
[3] S.H. Won, B. Jiang, P. Diévart, C.H. Sohn, Y. Ju, Self-sustaining n-heptane cool diffusion flames activated by ozone, Proc. Combust. Inst. 35 (2015) 881–888.
[4] J.F. Griffiths, S.K. Scott, Thermokinetic interactions: fundamentals of spontaneous ignition and cool flames, Prog. Energy Combust. Sci. 13 (1987) 161–197.
[5] G. Paczko, N. Peters, K. Seshadri, F.A. Williams, The role of cool-flame chemistry in quasi-steady combustion and extinction of n-heptane droplets, Combust. Theory Model. 18 (2014) 515–531.
[6] V. Nayagam, D.L. Dietrich, P.V. Ferkul, M.C. Hicks, F.A. Williams, Can cool flames support quasi-steady alkane droplet burning? Combust. Flame 159 (2012) 3583–3588.
[7] T.I. Farouk, F.L. Dryer, Isolated n-heptane droplet combustion in microgravity: "Cool Flames" – Two-stage combustion, Combust. Flame 161 (2014) 565–581.
[8] C.K. Law, P. Zhao, NTC-affected ignition in nonpremixed counterflow, Combust. Flame 159 (2012) 1044–1054.
[9] R.D. Reitz, Directions in internal combustion engine research, Combust. Flame 160 (2013) 1–8.
[10] S. Deng, D. Han, C.K. Law, Ignition and extinction of strained nonpremixed cool flames at elevated pressures, Combust. Flame. 176 (2017) 143–150.
[11] T.I. Farouk, D. Dietrich, F.E. Alam, F.L. Dryer, Isolated n-decane droplet combustion – dual stage and single stage transition to "Cool Flame" droplet burning, Proc. Combust. Inst. 36 (2017) 2523–2530.
[12] V. Nayagam, D.L. Dietrich, M.C. Hicks, F.A. Williams, Cool-flame extinction during n-alkane droplet combustion in microgravity, Combust. Flame. 162 (2015) 2140–2147.
[13] D.L. Dietrich, R. Calabria, P. Massoli, V. Nayagam, F.A. Williams, Experimental observations of the low-temperature burning of decane/hexanol droplets in microgravity, Combust. Sci. Technol. 189 (2017) 520–554.
[14] T.I. Farouk, D. Dietrich, F.L. Dryer, Three stage cool flame droplet burning behavior of n-alkane droplets at elevated pressure conditions: hot, warm and cool flame, Proc. Combust. Inst. 37 (2019) 3353–3361.
[15] V. Nayagam, D.L. Dietrich, F.A. Williams, Effects of properties of atmosphere diluents on cool-flame combustion of normal-alkane droplets, Combust. Flame. 229 (2021) 111408.
[16] X.L. Zheng, T.F. Lu, C.K. Law, C.K. Westbrook, H.J. Curran, Experimental and computational study of nonpremixed ignition of dimethyl ether in counterflow, Proc. Combust. Inst. 30 (2005) 1101–1109.
[17] W. Sun, S.H. Won, Y. Ju, In situ plasma activated low temperature chemistry and the S-curve transition in DME/oxygen/helium mixture, Combust. Flame. 161 (2014) 2054–2063.
[18] C.B. Reuter, M. Lee, S.H. Won, Y. Ju, Study of the low-temperature reactivity of large n-alkanes through cool diffusion flame extinction, Combust. Flame. 179 (2017) 23–32.
[19] A. Alfazazi, A. Al-Omier, A. Secco, H. Selim, Y. Ju, S.M. Sarathy, Cool diffusion flames of butane isomers activated by ozone in the counterflow, Combust. Flame. 191 (2018) 175–186.
[20] Y. Murakami, C.B. Reuter, O.R. Yehia, Y. Ju, Studies of autoignition-assisted nonpremixed cool flames, Proc. Combust. Inst. 38 (2021) 2333–2340.

[21] O.R. Yehia, C.B. Reuter, Y. Ju, Low-temperature multistage warm diffusion flames, Combust. Flame. 195 (2018) 63–74.
[22] O.R. Yehia, C.B. Reuter, Y. Ju, On the chemical characteristics and dynamics of n-alkane low-temperature multistage diffusion flames, Proc. Combust. Inst. 37 (2019) 1717–1724.
[23] Y. Kang, Q. Wang, P. Zhang, C. Liu, X. Lu, Q. Wang, Study on flame structure and extinction mechanism of dimethyl ether spherical diffusion flames, Energy 193 (2020) 116786.
[24] P. Zhang, Y. Kang, X. Huang, S. Peng, Comparative study on the dimethyl ether combustion characteristics in normal and inverse diffusion spherical flame geometries, ACS Omega 5 (2020) 24654–24665.
[25] A.G. Novoselov, C.B. Reuter, O.R. Yehia, S.H. Won, M.K. Fu, K. Kokmanian, M. Hultmark, Y. Ju, M.E. Mueller, Turbulent nonpremixed cool flames: experimental measurements, direct numerical simulation, and manifold-based combustion modeling, Combust. Flame. 209 (2019) 144–154.
[26] P.H. Irace, H.J. Lee, K. Waddell, L. Tan, D.P. Stocker, P.B. Sunderland, R.L. Axelbaum, Observations of long duration microgravity spherical diffusion flames aboard the international space station, Combust. Flame. 229 (2021) 111373.
[27] P. Dehghani, P.B. Sunderland, J.G. Quintiere, J.L. deRis, Burning in microgravity: experimental results and analysis, Combust. Flame. 228 (2021) 315–330.
[28] V. Nayagam, D.L. Dietrich, F.A. Williams, Partial-burning regime for quasi-steady droplet combustion supported by cool flames, AIAA J 54 (2016) 1235–1239.
[29] D.L. Dietrich, V. Nayagam, M.C. Hicks, P.V. Ferkul, F.L. Dryer, T. Farouk, B.D. Shaw, H.K. Suh, M.Y. Choi, Y.C. Liu, C.T. Avedisian, F.A. Williams, Droplet combustion experiments aboard the international space station, Microgravity Sci. Technol. 26 (2014) 65–76.
[30] K. Seshadri, N. Peters, F.A. Williams, V. Nayagam, G. Paczko, Asymptotic analysis of quasi-steady n-heptane droplet combustion supported by cool-flame chemistry, Combust. Theory Model. 20 (2016) 1118–1130.
[31] A. Cuoci, A.E. Saufi, A. Frassoldati, D.L. Dietrich, F.A. Williams, T. Faravelli, Flame extinction and low-temperature combustion of isolated fuel droplets of n-alkanes, Proc. Combust. Inst. 36 (2017) 2531–2539.
[32] M. Kim, Spherical Gas-Fueled Cool Diffusion Flames, University of Maryland, 2022 M.S. thesis.
[33] M. Lee, Y. Fan, Y. Ju, Y. Suzuki, Ignition characteristics of premixed cool flames on a heated wall, Combust. Flame. 231 (2021) 111476.
[34] J.C. Prince, F.A. Williams, Short chemical-kinetic mechanisms for low-temperature ignition of propane and ethane, Combust. Flame. 159 (2012) 2336–2344.
[35] F.A. Williams, V. Nayagam, Quasi-steady combustion of normal-alkane droplets supported by Cool-Flame chemistry near diffusive extinction, Combust. Theory Model. 23 (2019) 748–770.
[36] Z. Wang, P.B. Sunderland, R.L. Axelbaum, Dilution effects on laminar jet diffusion flame lengths, Proc. Combust. Inst. 37 (2019) 1547–1553.